ACSNANO
www.acsnano.org
ARTICLE

Secondary Electron Imaging of Light at the Nanoscale

Moshik Cohen,*[,†,‡,§] Yossi Abulafia,[‡] Reuven Shavit,[§] and Zeev Zalevsky[†,‡]

[†]Faculty of Engineering and [‡]Institute for Nanotechnology and Advanced Materials, Bar-Ilan University, Ramat-Gan 52900, Israel
[§]Department of Electrical and Computer Engineering, Ben-Gurion University of the Negev, Beer-Sheva 84105, Israel

Supporting Information

ABSTRACT: **The interaction of fast electrons with metal atoms may lead to optical excitations. This exciting phenomenon forms the basis for the most powerful inspection methods in nanotechnology, such as cathodoluminescence and electron−energy loss spectroscopy. However, direct nanoimaging of light based on electrons is yet to be introduced. Here, we experimentally demonstrate simultaneous excitation and nanoimaging of optical signals using unmodified scanning electron microscope. We use high-energy electron beam for plasmon excitation and rapidly image the optical near fields using the emitted secondary electrons. We analyze dipole nanoantennas coupled with channel nanoplasmonic waveguides and observe both surface plasmons and surface plasmon polaritons with spatial resolution of 25 nm. Our experimental results are confirmed by rigorous numerical calculations based on full-wave solution of Maxwell's equations, showing high correlation between optical near fields and secondary electrons images. This demonstration of optical near-field mapping using direct electron imaging provides essential insights to the exciting relations between electrons plasmons and photons, paving the way toward secondary electron-based plasmon analysis at the nanoscale.**

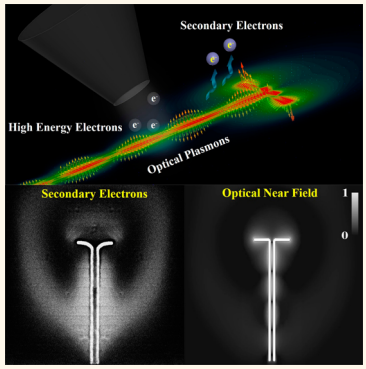

KEYWORDS: *scanning electron microscopy, plasmonics, photonics, nanoimaging, nanoantennas, plasmon waveguides*

Surface plasmon polaritons (SPPs) are optically excited charge density waves, propagating along metal−dielectric interfaces.[1] Surface plasmon nanophotonics grants the speed and bandwidth of photonics with dimensions of integrated electronics and enables light−matter interaction on a deep nanoscale.[2−4] These properties have recently propelled a rapid extension of interest from both fundamental and applicative perspectives. This includes ultrafast nanophotonics,[4−6] solar energy conversion,[7−9] biomedical sensing and imaging,[10−13] as well as superlensing[12,14,15] and metasurface holography.[16] Characterization of optical plasmons requires proper excitation and detection schemes. Excitation of SP is usually performed optically and requires momentum matching devices as prisms,[17] gratings,[18] or nanoantennas.[19] Unfortunately, these techniques do not easily allow for a high localization and accurate positioning of the radiation source. In contrast, plasmons can be generated using irradiation with electron beam, inherently enabling excitation with nanoscale resolution.[20−22] Detection of SP can be realized on both optical and electrical domains. Optical nanoimaging is commonly performed using scanning near-field optical microscope (SNOM), where the probe is used for direct collection of the field in aperture mode[23] or used as a scatterer in scattering SNOM (s-SNOM).[24] Optical detection is also enabled by coupling the plasmons to radiating photons and using diffraction limited optics,[25] as the combination of electrical excitation with far field optical detection is demonstrated *via* cathodoluminescence (CL).[20,26−28] Indirect electrical detection of SPPs at the far field was reported using electron energy loss spectroscopy (EELS),[29−31] with time-resolved measurements demonstrated using laser excited photo cathodes in electric microscopy.[32,33] As CL and EELS use an electron beam of a scanning electron microscope (SEM) for plasmons excitation, both require large dwell times[34−36] and major modifications for optical imaging. In addition to standard SEM, CL requires parabolic mirror and CL spectrograph, as EELS mostly involves transmission electron microscopy (TEM), electron spectrometer, and a monochromator.[37−39] Recently reported approaches for direct-electron-based plasmon nanoimaging include Kelvin probe force microscopy (KPFM)[4,40−42] and photoemission electron microscopy (PEEM).[43−46] Both methods require optical illumination, where KPFM maps the surface work function and PEEM images the emitted electrons. In SEM, a tightly focused electron beam with energies typically up to 50 keV hits the specimen to excite various signals, which mainly include secondary electrons emission (SEE), high-energy backscattered electrons, and characteristic X-rays. Secondary electron-based SEM, the basis for our experimental measurements, is essential in a huge variety of applications including

Received: January 24, 2017
Accepted: March 6, 2017
Published: March 6, 2017

DOI: 10.1021/acsnano.7b00548
ACS Nano 2017, 11, 3274−3281

high-resolution surface potential imaging,[47] stem cell studies,[48] biomedical imaging,[49−51] and topography examination of nanostructures.[4,25,40] In this work, we experimentally demonstrate direct excitation and nanoimaging of optical signals, entirely based on unmodified SEM. As illustrated in Figure 1,

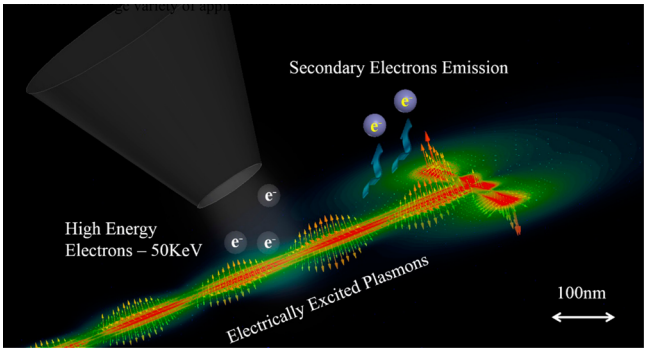

Figure 1. Illustration of electron-based plasmon generation and imaging in SEM. A high-energy electron beam illuminates the device, a nanoantenna coupled with channel waveguide. Optical plasmons are excited and decay to generate the emitted secondary electrons.

we use an electron beam as a nanoscale source of electromagnetic radiation and base our optical mapping on the emitted secondary electrons. We ascertain that the resulted near-field images are dependent on the sample conditions and discuss appropriate fabrication considerations. Our approach provides rapid intensity maps (1 μS/pixel) of optical near fields, with decreased sensitivity to nanofabrication inaccuracies due to the broad spectral nature of the electron beam. We image SPPs in channel plasmon waveguides with a slot width varying between 20 nm and 60 nm, in addition to localized plasmons excited at a variety of dipole nanoantennas and optical surface waves on dielectric substrates. Broadband SPP mode properties and antenna emission patterns are imaged with deep subwavelength resolution. Our experimental results are in excellent agreement with electromagnetic calculations, based on a 3D numerical solution of Maxwell's equations. Furthermore, we present an analytic description for the excitation of SPPs by swift electrons and provide a semi-empirical estimation for the plasmon contribution to the SEE. The theoretical origin of this work lies in the fact that the passage of a fast electron can excite localized plasmons in metallic nanoparticles as well as SPPs on planar metallic surfaces or in metal nanowires.[52−54] These plasmons can partially decay *via* inelastic channels that involve electronic excitations, including $e-h$ pair creation and SEE.[54−57]

The electromagnetic field of a point charge moving in vacuum can be regarded as an evanescent source of radiation that permits exploring regions of momentum−energy space that lie outside the light cone. For swift electrons with a constant velocity, ϑ, and a momentum k that interact with a thin specimen, the frequency domain electron charge density becomes $-2\pi\delta(\omega - k \times v)$, where $\omega = 2\pi f$ is the angular frequency. This approximation is well suited for our experimental conditions, which include 25 nm-thick metallic devices bombarded by 50 keV electron beam. Hence, we can obtain the electromagnetic fields produced by a swiftly charged particle moving inside a homogeneous medium by a direct solution of Maxwell's equations in the frequency−momentum space. Specifically, the electric field as a function of distance R from the beam takes the form of[54] (for detailed derivation, see Supporting Information)

$$\mathbf{E}_j^{\text{bulk}}(\mathbf{r}, \omega) = \frac{2e\omega}{v^2\varepsilon\gamma} e^{i\omega z/v}\left[\frac{i}{\gamma_e}K_0(u)\hat{z} - K_1(u)\hat{\rho}\right] \quad (1)$$

where $\gamma_e = (1 - \vartheta^2/c^2)^{-0.5}$ is the Lorentz contraction factor, ω is the angular frequency, $r = (\rho, z)$ and $u = \omega R/\vartheta\gamma_e$. The modified Bessel functions K_m describe an exponential decay of the field intensity with R for $\omega R/\vartheta\gamma_e > 0.2$.[54] Hence, we see that the moving electron acts as a broadband source of electromagnetic radiation, with the frequency components of the field moving with velocity ϑ along the electron trajectory. Using boundary conditions for the electromagnetic fields at the interfaces, we obtain the SPP excitation probability for incident electron beam with energies of 50 keV and 100 keV,[52,54] shown in Figure 2a (Figure 2a implements eq 19 in the Supporting Information).

In metals, secondary electronic excitations establish a dominant decay channel for localized and propagating plasmons, capable of producing electrons above the vacuum level that contribute to the detected SEE.[54−56] Both ion[58−60] and electron beam[55−57] induced plasmon assisted secondary electron emissions from metals were extensively investigated. Detailed analytical formulation of plasmon decay role in

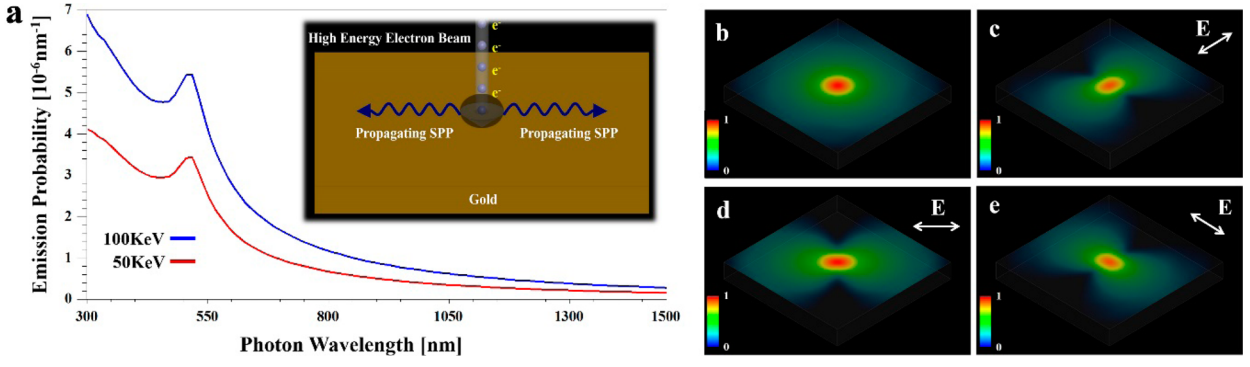

Figure 2. Plasmon excitation *via* electron beam-theoretical analysis. (a) Generation rate of SPP as a function of wavelength per incoming electron. The rates are calculated for 50 keV (red) and 100 keV (blue) electrons incident on a gold surface. Inset: the analyzed geometry (b). Numerical calculation of an optically modeled electron beam (50 keV, 1 nm radius), illuminating the geometry described in (a), showing the electric-field magnitude |E| on the surface (c). Numerically calculated |E| for a linearly polarized broad optical source at 45° polarization angle (d). Excitation with horizontal polarization (e). Excitation with linear polarization with −45° polarization angle.

DOI: 10.1021/acsnano.7b00548
ACS Nano 2017, 11, 3274−3281

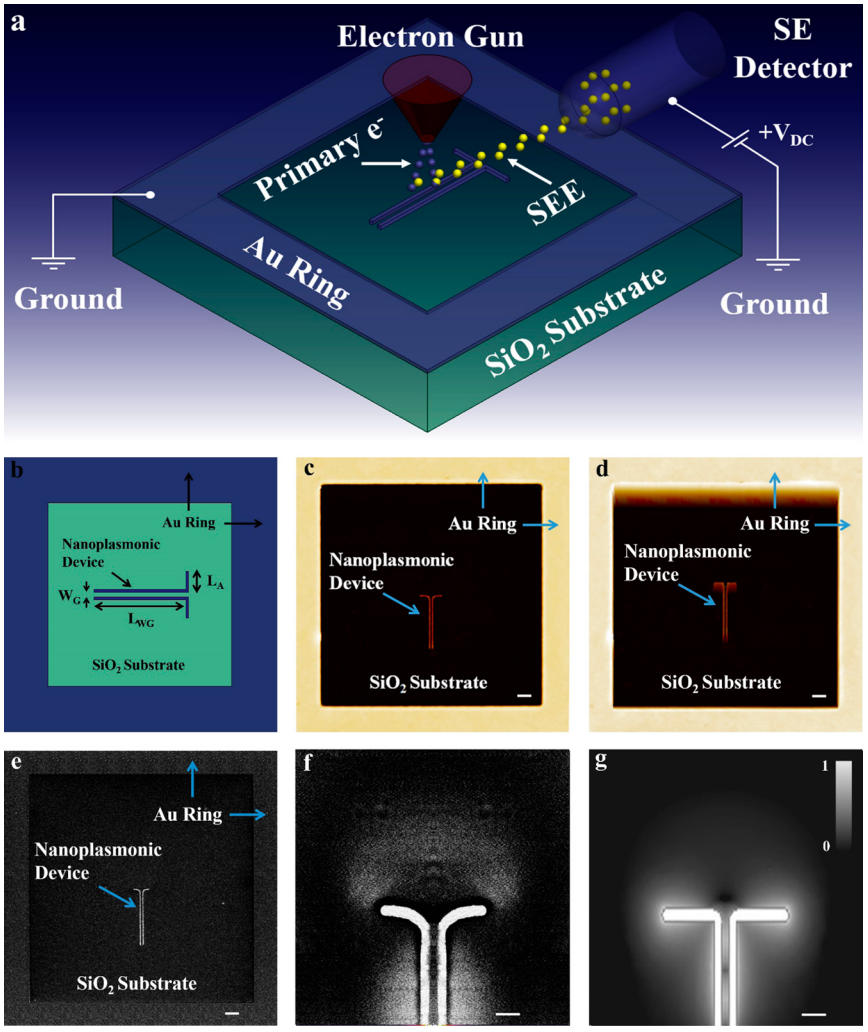

Figure 3. Electrical excitation and imaging of optical nanoplasmons. (a) Schematic illustration of our experimental setup. (b) Description of the analyzed nanoplasmonic devices. Dipole nanoantenna with an arm length 'L_A' and gap 'W_G', connected to a channel waveguide of length L_{WG}. The devices are made of Au on a SiO_2 substrate and surrounded by a Au square ring, which controlled the SE emission rate toward the detector. (c) 2D high-resolution AFM topography map of the analyzed device. (d) 3D high-resolution AFM topography map of the device. (e) SEM topography mapping of an identical device obtained with low beam energy (5 keV) and current (25 pA). (f) SEM (SEE) response of the device under excitation *via* high energy, focused electron beam (50keV, 1 nm). (g) 3D numerical simulation showing the electric-field magnitude |E| of the device, when excited by a 50 keV, 1 nm electron beam. Scale bar: 100 nm.

secondary electron emission in the nearly free-electron metals was reported,[55] showing a strong dependency on the incident beam angle and electron velocity. In this work, we use a normal incident angle, with incident electron velocity corresponding to an accelerating voltage (V) of 5− 50 keV ($\theta = 90°$; $\vartheta_0 = (2\ eV/m)^{0.5}$, see ref 54). The metals in use are described by their in plane complex dielectric function ($\varepsilon_{\parallel} \equiv \varepsilon_r + i\varepsilon_i$) using the Drude model, which gives good agreement for Au within the 300−1200 nm wavelength range.[61] Since $\omega \gg \Gamma \sim 1 \times 10^{13}$ ($\Gamma = 1/\tau$ is the damping rate constant), the in plane relative permittivity can be written as $\varepsilon_{\parallel} = \varepsilon_B - \omega_p^2/\omega^2 + i\omega_p^3/\omega^2\tau$, where ε_B is the contribution of bound electrons and ω_p is the plasma frequency.[40] The numerical calculations are performed using the finite element method (FEM) solution of Maxwell's equations (HFSS V15).[4,15,40] The electron beam was modeled (using eq 1) as a broadband source of electromagnetic radiation ranging from 300−1000 THz in frequency steps of 20 THz. The unpolarized[54] nature of the electron beam was modeled by incoherently summing the results from two separated calculations performed with orthogonal, linearly polarized sources using $|E|^2 = 0.5|\vec{E}_s|^2 + 0.5|\vec{E}_p|^2$. The quantity $|E|^2$ is the time averaged electric field intensity of the unpolarized beam source, $\vec{E}_s$ and $\vec{E}_p$ are the horizontally and vertically polarized sources, respectively (for a detailed derivation, see Supporting Information). Figure 2b−e presents simulation results of the electric field generated from an optically modeled high-energy (50 keV) electron beam impinging on Au−air interface, showing the frequency-aggregated electric-field magnitude, $|\mathbf{E}| = 1/N\sum_{\omega_1}^{\omega_N}|\mathbf{E}(\omega_i)|$. To enable excitation of SPPs, we created a subwavelength circular aperture of 50 nm radius at the center of the Au sample.[1] Figure 2b shows |E| for an electron beam excitation, with polarization-dependent results shown for different states in Figure 2c−e. As expected, a localized hot spot appears at the circular interface, followed by SPP propagation with respect to the electric-field polarization. The experimental setup used in this work is schematically illustrated in Figure 3a. Our image formation process is identical to the broadly used SEM for topography mapping.[62−66] To form the image, high-energy electrons are focused into a fine beam,

DOI: 10.1021/acsnano.7b00548
ACS Nano 2017, 11, 3274−3281

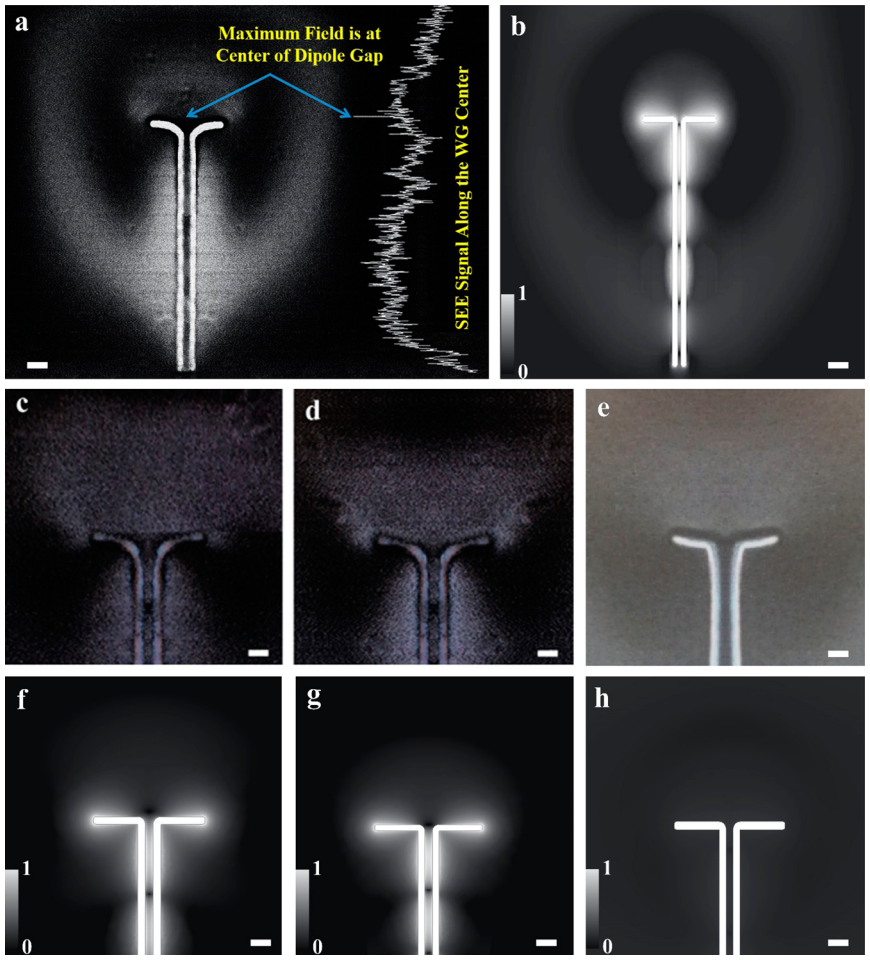

Figure 4. Optical near-field nanoimaging base on SEE. (a) SE imaging of the device, excited by a high impact-focused (50keV, 1 nm) electron beam. The field along the yellow line is shown in decibels (dB) at the right. (b) 3D numerical simulation showing the electric-field magnitude |E| of the device in (a). (c) SEE map of a device designed for resonance at 530 nm, under excitation *via* electron beam (50keV, 1 nm). (d) SEE map of a device designed for off-resonance behavior, under excitation *via* electron beam (50keV, 1 nm). (e) SEE map of the device in (d) excitation *via* 10keV electron beam. (f–h) Numerically calculated |E| of the device in (c–e), respectively. Scale bar: 100 nm.

which is scanned across the surface of the specimen. For each illuminated pixel, a positively biased-synchronized detector collects the excited SE and produces the image by mapping the operation that transmits information from the specimen space to the display space with controlled time averaging. We show that the SE fields can have the shape and dispersion properties of both plasmons and surface photons. We investigate hybrid devices of dipole nanoantennas integrated with channel plasmonic waveguides as shown in Figure 3b.

In addition to their importance for a large variety of applications,[4,15,40] analyzing these devices enables the mapping of both localized and propagating plasmons. The structures where fabricated on a SOI substrate by electron beam lithography (EBL), ion beam sputtering (Cr, 3 nm Au, 22 nm), and lift off. To minimize the effects of conventional charging on the field patterns, we chose the well-known approach of designing an intrinsically high-conductivity sample.[67−69] Hence, the devices were fabricated inside square apertures with dimensions of 6 μm × 6 μm; keeping over 99.9% of the sample surface as grounded Au (see Figure 1 and Supporting Information). The 6 μm × 6 μm aperture dimensions were chosen empirically to provide the highest quality images. To verify the fabrication process, we investigated the samples using high-resolution atomic force microscopy (AFM) with a tip diameter of 5 nm. Figure 3c,d, respectively, presents 2D and 3D topography images of the fabricated device, with geometrical dimensions of L_{WG} = 1500 nm, L_A = 200 nm, and W_G = 25 nm. The AFM study confirms the success of our fabrication process, showing clean waveguide channels and almost no residual particles in the regions of interest. The metallic square frame surrounding the device is also captured. Figure 3e shows topography mapping of the analyzed device, obtained using SEM at low (5keV) beam energy. The topography resembles the 2D AFM image, with no additional signals observed along the sample besides those that correspond to the actual device structure. However, when the beam energy is increased above a few tens of keV, optical plasmons are excited at the metal−dielectric interfaces along the device. These plasmons partially decay and transfer their energy to produce SE.[54−56] Figure 3f shows the nanoplasmonic device under excitation with a high-energy (50keV) electron beam, focused to 1 nm radius. Alongside the device topography, we observe enhanced fields at the metal−dielectric interfaces, which arise from plasmon excitation along the device. Additionally, the well-known dipolar optical-field pattern emitted from the nanoantenna[4,40] is clearly captured in the SE image. The experimental results are strongly supported by numerical calculations. The calculated electric-field magnitude, |

DOI: 10.1021/acsnano.7b00548
ACS Nano 2017, 11, 3274−3281

|E|, which is proportional to the SE excitation efficiency,[55−58] is shown in Figure 3g. Similar to the SE map, dipolar emission pattern from the nanoantenna as well as plasmonic enhancement at the metallic interfaces are well observed. Figure 4 shows quantitative analysis of the plasmonic devices with nanoscale resolution and broad frequency range. Figure 4a presents a 2D SE field map of the analyzed structure, where the field along the waveguide center is shown at the right-hand side of the device in logarithmic scale. The SE field along the waveguide center shows a standing wave pattern with the maximum field intensity located exactly at the nanoantenna gap, represented by a strong peak in the SE signal as expected for similar devices.[4,40,41] The field outside the device shows a different behavior, where the dipolar shaped emission is coupled to the surface and forms a standing wave pattern, exponentially decaying as a function of the distance from the metallic structure. The corresponding optical calculation of the electron image is shown in Figure 4b. The experiments and theoretical calculations are of high correlation, providing direct evidence to the coupling of both surface photons and free electrons from the nanoantenna to the sample surface, with directive propagation governed by the emission pattern. We note that a few of the oscillatory fields observed in Figure 4a do not appear in Figure 4b, mainly due to the non-continuous nature of the FEM calculations, where each frequency component excites the oscillatory mode.[40] Improved calculation results will be obtained by using time domain methods (FDTD) or increasing the frequency-sampling rate. Figure 4c shows the SEE field map for a device designed for resonance at the wavelength that maximizes plasmon excitation probability (Figure 2a), with corresponding dimensions of L_A = 180 nm, W_G = 25 nm. The SEE map for an off-resonance device (L_A = 210 nm, W_G = 30 nm) is shown in Figure 4d. The corresponding calculated |E| is presented in Figure 4f,g, respectively. The resonance device shows a 4 dB stronger field enhancement at the nanoantenna gap, and its emitted field extends significantly more into the substrate compared with the off-resonance device. The plasmons are coupled to optical surface waves also from the exterior waveguide interfaces, as observed in both experimental and calculation results. To provide additional evidence for the proficiency of the proposed method, we recorded SEE maps of the device excited with lower beam energy. Figure 4e shows the SEE analysis of the device in Figure 4d, captured with a beam energy of 10keV, with the corresponding calculation results shown in Figure 4h. As expected, the plasmon generation is significantly less pronounced compared to the case of excitation with the 50 keV beam, supported by both theory and experiments. To quantify the plasmon contribution to the SE signal, we characterize similar devices fabricated from SiO_2, a dielectric material that does not support plasmon excitation. Figure 5a shows an SE image of the SiO_2 device captured under identical conditions to the described experiments above, with the corresponding calculated |E| shown in Figure 5b. As expected, enhanced SE is observed only from the device topography with no additional SE signals detected; unlike the case of the plasmonic (Au) device. This shows that the enhanced SEE outside the device topography is mainly material related, which results in excited optical plasmons. For each pixel, the quotient of SE signals from the plasmonic (Figure 4c) and dielectric (Figure 5a) devices is the plasmon contribution to the SEE. For our images, the described ratio varies between 1.5 dB and 23 dB (for a dwell time of 1 μS per pixel). This means that the plasmon contribution enhances the SE emission by a factor varying from 1.4 to 200. Figure 5c shows a SE map of the plasmonic device, where the field along the dipole axis (yellow line) is presented. Note that the measured signal level at the right interface is slightly higher compared to the left interface, attributed to nanofabrication inaccuracy. The field contributions from the left (LI) and right (RI) dipole interfaces are clearly resolved, demonstrating spatial resolution in the region of 25 nm. We suggest several effects originated in the SE detector, which may possibly contribute to the minor differences between the experimental and theoretical SE images. The SE detector is located at a distance of ∼54 mm from the analyzed specimen with a relative angle of 21° (see also Figure S6); this relative position may create a shift in both delay and spatial distribution of the SE hitting the detector in comparison to their real values. In addition, finite signal-to-noise ratio and dynamic range of the detector (measured to be approximately 15 and 30 dB, respectively) may add to the slight smearing of the waves observed in the experimental SEE maps and does not appear in the numerically calculated images.

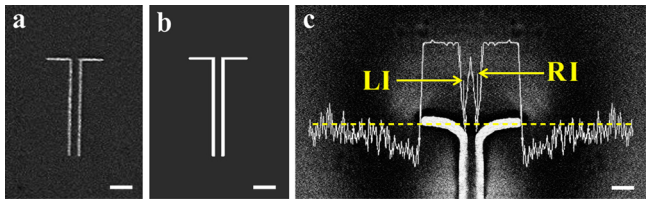

Figure 5. Control experiment and demonstration of the SEE spatial resolution. (a) SEE analysis of a similar device as in Figure 4a fabricated from SiO_2. (b) 3D numerical simulation showing the electric-field magnitude |E| of the device in (a). (c) SEE analysis of the plasmonic device excited by a 50 keV electron beam. The field along the dashed yellow line is presented, showing the capability of the SEM to resolve the field contribution of the left (LI) and the right (RI) waveguide interfaces, separated by 25 nm. Scale bars: (a, b) 100 nm; (c) 50 nm.

CONCLUSIONS

In summary, we introduce an approach for optical excitation and nanoimaging based on unmodified secondary electron microscopy. The proposed method facilitates ultrafast, simultaneous mapping of optical near fields and device topography, with both displayed in a single image. Based on secondary electrons as the fundamental imaging particle, our proposed method enables high spatial resolution; potentially outperforms the 25 nm resolution experimentally demonstrated in this work. Our experimental results are confirmed by rigorous numerical calculations, showing good agreement between secondary electron field maps and optical near fields, and offer rare insights into the tight relations between electrons photons and plasmons. Our findings provide the path for fundamental and applicative horizons of electron beam plasmonics, such as ultrafast broadband nanoimaging, molecular energy transfer, and optically inspired secondary electron cloaking.

METHODS

Devices Fabrication. The SOI sample was spin-coated with poly(methyl methacrylate) (PMMA 950 A2) by electron-beam resist, providing a thickness of 100 nm. The samples coated with PMMA were subsequently baked for 120 s on a hot plate at 180C. The desired pattern was exposed in the PMMA layer using a CRESTEC CABLE-

DOI: 10.1021/acsnano.7b00548
ACS Nano 2017, 11, 3274−3281

9000C high-resolution electron-beam lithography system using different doses to control line and gap widths. Then the samples were developed for 90 s using "methyl isobutyl ketone" (MIBK) and rinsed with IPA. The samples were subsequently exposed to Ar plasma to etch 10 nm in order to remove leftovers from the pattern, sputtered using BESTEC 2″ DC magnetron to deposit 3 nm Cr and 22 nm Au, and then immersed in 180 kHz ultrasonic bath with NMP for 3 h for resist liftoff.

SEM Characterization. Both topography and functional measurements were carried out simultaneously using a CRESTEC CABLE-9000C high-resolution electron-beam lithography system with integrated SEM, with vacuum levels of ∼10−5. The samples surface (Au) was grounded to zero DC potential, as it was vector scanned (x,y) using a high-energy (50 keV) electron beam, focused to 1 nm radius with controllable beam currents varied between 5 pA and 250 pA. We used nominal scan rates of 50−200 mS/frame for analog and digital scans. The emitted secondary electrons were collected *via* SE detector, biased to 10 kV. In our experiments, the horizontal (x) axis is defined as the "fast axis", with the vertical (y) is the slow axis. To reduce noise and increase the image resolution, we used a pixel averaging of 4 points per pixel as well as frame averaging of four frames per image. Combined pixel and frame averaging reduces the effects of high and low spatial frequency noises, respectively. All of the SEM images, micrograph, intensities, and counts in this work are presented in logarithmic scale.

AFM Measurements. All measurements were performed at room temperature and free ambient conditions (no vacuum), using a Dimension Icon AFM system with NanoScope V controller (Bruker). We used NanoWorld probes SSS-NCH, SuperSharpSilicon - Non-contact/Tapping mode - high resonance frequency, with a typical diameter of 2 nm, resonance frequency of 320 kHz, and spring constant of 42 N/m.

Numerical Simulations. The numerical results are obtained by using the software package ANSYS HFSS V15, the industry standard simulation tool for 3D full-wave electromagnetic-field simulation. HFSS solves Maxwell's equations *via* the finite element method (FEM) using an adaptive mesh refinement process for tailored accuracy requirements. The field's solutions are calculated with the metallic (Au) plasmonic structures being deposited on a homogeneous SiO_2 substrate. The sample is illuminated by optical source at spectral range of 300−1000 THz, which is modeled as a focused beam with 1 nm characteristic radius. The electric field is of controlled polarization as the wave vector K is normal to the surface. A selectively dense meshing is assigned in the metallic and waveguiding regions, with a maximum cell size of 1 nm and 750,000 FEM tetrahedral cells. To provide maximum accuracy, the model is terminated as follows: The interface with free space is bounded by a broad band perfectly matched layer (PML) absorbing boundary conditions (ABC), while the metallic and SiO_2 terminations are done *via* layered impedance (LI) ABC. The minimum number of adaptive meshing iterations was set to 12, with a convergence condition of 1% maximum energy variance between adjacent iterations.

ASSOCIATED CONTENT

Supporting Information

The Supporting Information is available free of charge on the ACS Publications website at DOI: 10.1021/acsnano.7b00548.

Detailed derivation of the analytical formulation of an electron beam radiation source and its associated electromagnetic fields; sample design for minimization of charging effects; and additional experiments conducted with scanning axis rotation (PDF)

AUTHOR INFORMATION

Corresponding Author

*E-mail: moshik.cohen80@gmail.com.

ORCID

Moshik Cohen: 0000-0002-7519-9742

Author Contributions

M.C. initiated and designed the studies, carried out the theoretical design and analysis, performed the experiments, and wrote the manuscript. Y.A. fabricated the devices and performed the experiments. R.S. contributed the computational facility. Z.Z. reviewed the manuscript and participated in the results analysis.

Funding

The authors declare that no funding was provided for any of the authors for this work.

Notes

The authors declare no competing financial interest.

ACKNOWLEDGMENTS

M.C acknowledges Prof. Javier Garcia De Abajo for the great discussions, enhancing the authors understanding and knowledge in this fascinating field.

REFERENCES

(1) Pitarke, J. M.; Silkin, V. M.; Chulkov, E. V.; Echenique, P. M. Theory of Surface Plasmons and Surface-Plasmon Polaritons. *Rep. Prog. Phys.* **2007**, *70*, 1.

(2) Brongersma, M. L.; Shalaev, V. M. The Case for Plasmonics. *Science* **2010**, *328*, 440−441.

(3) Gramotnev, D. K.; Bozhevolnyi, S. I. Plasmonics beyond the Diffraction Limit. *Nat. Photonics* **2010**, *4*, 83−91.

(4) Cohen, M.; Zalevsky, Z.; Shavit, R. Towards Integrated Nanoplasmonic Logic Circuitry. *Nanoscale* **2013**, *5*, 5442.

(5) Wurtz, G. A.; Pollard, R.; Hendren, W.; Wiederrecht, G. P.; Gosztola, D. J.; Podolskiy, V. A.; Zayats, A. V. Designed Ultrafast Optical Nonlinearity in a Plasmonic Nanorod Metamaterial Enhanced by Nonlocality. *Nat. Nanotechnol.* **2011**, *6*, 107−111.

(6) Pohl, M.; Belotelov, V. I.; Akimov, I. A.; Kasture, S.; Vengurlekar, A. S.; Gopal, A. V.; Zvezdin, A. K.; Yakovlev, D. R.; Bayer, M. Plasmonic Crystals for Ultrafast Nanophotonics: Optical Switching of Surface Plasmon Polaritons. *Phys. Rev. B: Condens. Matter Mater. Phys.* **2012**, *85*, 81401.

(7) Atwater, H. A.; Polman, A. Plasmonics for Improved Photovoltaic Devices. *Nat. Mater.* **2010**, *9*, 205−213.

(8) Echtermeyer, T. J.; Britnell, L.; Jasnos, P. K.; Lombardo, A.; Gorbachev, R. V.; Grigorenko, A. N.; Geim, A. K.; Ferrari, A. C.; Novoselov, K. S. Strong Plasmonic Enhancement of Photovoltage in Graphene. *Nat. Commun.* **2011**, *2*, 458.

(9) Green, M. A.; Pillai, S. Harnessing Plasmonics for Solar Cells. *Nat. Photonics* **2012**, *6*, 130−132.

(10) Anker, J. N.; Hall, W. P.; Lyandres, O.; Shah, N. C.; Zhao, J.; Van Duyne, R. P. Biosensing with Plasmonic Nanosensors. *Nat. Mater.* **2008**, *7*, 442−453.

(11) Feng, J.; Siu, V. S.; Roelke, A.; Mehta, V.; Rhieu, S. Y.; Palmore, G. T. R.; Pacifici, D. Nanoscale Plasmonic Interferometers for Multispectral, High-Throughput Biochemical Sensing. *Nano Lett.* **2012**, *12*, 602−609.

(12) Kawata, S.; Inouye, Y.; Verma, P. Plasmonics for near-Field Nano-Imaging and Superlensing. *Nat. Photonics* **2009**, *3*, 388−394.

(13) Carmeli, I.; Cohen, M.; Heifler, O.; Lilach, Y.; Zalevsky, Z.; Mujica, V.; Richter, S. Spatial Modulation of Light Transmission through a Single Microcavity by Coupling of Photosynthetic Complex Excitations to Surface Plasmons. *Nat. Commun.* **2015**, *6*, 7334.

(14) Fang, N.; Lee, H.; Sun, C.; Zhang, X. Sub−Diffraction-Limited Optical Imaging with a Silver Superlens. *Science* **2005**, *308*, 534−537.

(15) Cohen, M.; Shavit, R.; Zalevsky, Z.; Abulafia, Y. Nanoplasmonic Phased Array Superlens with Extended Depth of Focus. Proceedings from *CLEO: Science and Innovations 2014*, San Jose, California, June

DOI: 10.1021/acsnano.7b00548
ACS Nano 2017, 11, 3274−3281

8–13, 2014; OSA Technical Digest (online); Optical Society of America: Washington, DC, 2014; p JTu4A.135.
(16) Ni, X.; Kildishev, A. V.; Shalaev, V. M. Metasurface Holograms for Visible Light. *Nat. Commun.* **2013**, *4*, 2807.
(17) Elston, S. J.; Sambles, J. R. Polarization Conversion Using Prism-Coupled Surface Plasmon-Polaritons. *J. Mod. Opt.* **1991**, *38*, 1223–1227.
(18) Boltasseva, A.; Bozhevolnyi, S. I.; Nikolajsen, T.; Leosson, K. Compact Bragg Gratings for Long-Range Surface Plasmon Polaritons. *J. Lightwave Technol.* **2006**, *24*, 912.
(19) Schnell, M.; Alonso-González, P.; Arzubiaga, L.; Casanova, F.; Hueso, L. E.; Chuvilin, A.; Hillenbrand, R. Nanofocusing of Mid-Infrared Energy with Tapered Transmission Lines. *Nat. Photonics* **2011**, *5*, 283–287.
(20) va Wijngaarden, J. T.; Verhagen, E.; Polman, A.; Ross, C. E.; Lezec, H. J.; Atwater, H. A. Direct Imaging of Propagation and Damping of near-Resonance Surface Plasmon Polaritons Using Cathodoluminescence Spectroscopy. *Appl. Phys. Lett.* **2006**, *88*, 221111.
(21) Adamo, G.; Ou, J. Y.; So, J. K.; Jenkins, S. D.; De Angelis, F.; MacDonald, K. F.; Di Fabrizio, E.; Ruostekoski, J.; Zheludev, N. I. Electron-Beam-Driven Collective-Mode Metamaterial Light Source. *Phys. Rev. Lett.* **2012**, *109*, 217401.
(22) Bashevoy, M. V.; Jonsson, F.; Krasavin, A. V.; Zheludev, N. I.; Chen, Y.; Stockman, M. I. Generation of Traveling Surface Plasmon Waves by Free-Electron Impact. *Nano Lett.* **2006**, *6*, 1113–1115.
(23) Zia, R.; Brongersma, M. L. Surface Plasmon Polariton Analogue to Young's Double-Slit Experiment. *Nat. Nanotechnol.* **2007**, *2*, 426–429.
(24) Chen, J.; Badioli, M.; Alonso-González, P.; Thongrattanasiri, S.; Huth, F.; Osmond, J.; Spasenović, M.; Centeno, A.; Pesquera, A.; Godignon, P.; Elorza, A.; Camara, N.; García de Abajo, F.; Hillenbrand, R.; Koppens, F H.L. Optical Nano-Imaging of Gate-Tunable Graphene Plasmons. *Nature* **2012**, *487*, 77–81.
(25) Fu, Y.; Hu, X.; Lu, C.; Yue, S.; Yang, H.; Gong, Q. All-Optical Logic Gates Based on Nanoscale Plasmonic Slot Waveguides. *Nano Lett.* **2012**, *12*, 5784–5790.
(26) Vesseur, E. J. R.; Coenen, T.; Caglayan, H.; Engheta, N.; Polman, A. Experimental Verification of n = 0 Structures for Visible Light. *Phys. Rev. Lett.* **2013**, *110*, 13902.
(27) Matter, A.; Ramseyer, K. Cathodoluminescence Microscopy as a Tool for Provenance Studies of Sandstones. In *Provenance of Arenites*; Zuffa, G. G., Ed.; NATO ASI Series; Springer: Netherlands, 1985; pp 191–211.
(28) Merano, M.; Sonderegger, S.; Crottini, A.; Collin, S.; Renucci, P.; Pelucchi, E.; Malko, A.; Baier, M. H.; Kapon, E.; Deveaud, B.; Ganière, J. D. Probing Carrier Dynamics in Nanostructures by Picosecond Cathodoluminescence. *Nature* **2005**, *438*, 479–482.
(29) Duan, H.; Fernández-Domínguez, A. I.; Bosman, M.; Maier, S. A.; Yang, J. K. W. Nanoplasmonics: Classical down to the Nanometer Scale. *Nano Lett.* **2012**, *12*, 1683–1689.
(30) Scholl, J. A.; García-Etxarri, A.; Koh, A. L.; Dionne, J. A. Observation of Quantum Tunneling between Two Plasmonic Nanoparticles. *Nano Lett.* **2013**, *13*, 564–569.
(31) Iberi, V.; Mirsaleh-Kohan, N.; Camden, J. P. Understanding Plasmonic Properties in Metallic Nanostructures by Correlating Photonic and Electronic Excitations. *J. Phys. Chem. Lett.* **2013**, *4*, 1070–1078.
(32) Zewail, A. H. Four-Dimensional Electron Microscopy. *Science* **2010**, *328*, 187–193.
(33) Kim, J. S.; LaGrange, T.; Reed, B. W.; Taheri, M. L.; Armstrong, M. R.; King, W. E.; Browning, N. D.; Campbell, G. H. Imaging of Transient Structures Using Nanosecond in Situ TEM. *Science* **2008**, *321*, 1472–1475.
(34) Takeuchi, K.; Yamamoto, N. Visualization of Surface Plasmon Polariton Waves in Two-Dimensional Plasmonic Crystal by Cathodoluminescence. *Opt. Express* **2011**, *19*, 12365.
(35) Zhu, X.; Zhang, J.; Xu, J.; Yu, D. Vertical Plasmonic Resonant Nanocavities. *Nano Lett.* **2011**, *11*, 1117–1121.
(36) Coenen, T.; Vesseur, E. J. R.; Polman, A.; Koenderink, A. F. Directional Emission from Plasmonic Yagi–Uda Antennas Probed by Angle-Resolved Cathodoluminescence Spectroscopy. *Nano Lett.* **2011**, *11*, 3779–3784.
(37) Myroshnychenko, V.; Nelayah, J.; Adamo, G.; Geuquet, N.; Rodríguez-Fernández, J.; Pastoriza-Santos, I.; MacDonald, K. F.; Henrard, L.; Liz-Marzán, L. M.; Zheludev, N. I.; Kociak, M.; Javier, G. A. F. Plasmon Spectroscopy and Imaging of Individual Gold Nanodecahedra: A Combined Optical Microscopy, Cathodoluminescence, and Electron Energy-Loss Spectroscopy Study. *Nano Lett.* **2012**, *12*, 4172–4180.
(38) Knight, M. W.; Liu, L.; Wang, Y.; Brown, L.; Mukherjee, S.; King, N. S.; Everitt, H. O.; Nordlander, P.; Halas, N. J. Aluminum Plasmonic Nanoantennas. *Nano Lett.* **2012**, *12*, 6000–6004.
(39) Chaturvedi, P.; Hsu, K. H.; Kumar, A.; Fung, K. H.; Mabon, J. C.; Fang, N. X. Imaging of Plasmonic Modes of Silver Nanoparticles Using High-Resolution Cathodoluminescence Spectroscopy. *ACS Nano* **2009**, *3*, 2965–2974.
(40) Cohen, M.; Shavit, R.; Zalevsky, Z. Observing Optical Plasmons on a Single Nanometer Scale. *Sci. Rep.* **2014**, *4*, 4096.
(41) Cohen, M.; Shavit, R.; Zalevsky, Z. Nanoplasmonic Metal–Insulator–Metal Waveguides. In *Planar Waveguides and other Confined Geometries*; Marowsky, G., Ed.; Springer Series in Optical Sciences; Springer: New York, 2015; pp 45–66.
(42) Cohen, M.; Shavit, R.; Zalevsky, Z. Enabling High Efficiency Nanoplasmonics with Novel Nanoantenna Architectures. *Sci. Rep.* **2015**, *5*, 17562.
(43) Aeschlimann, M.; Bauer, M.; Bayer, D.; Brixner, T.; García de Abajo, F. J.; Pfeiffer, W.; Rohmer, M.; Spindler, C.; Steeb, F. Adaptive Subwavelength Control of Nano-Optical Fields. *Nature* **2007**, *446*, 301–304.
(44) Kubo, A.; Onda, K.; Petek, H.; Sun, Z.; Jung, Y. S.; Kim, H. K. Femtosecond Imaging of Surface Plasmon Dynamics in a Nanostructured Silver Film. *Nano Lett.* **2005**, *5*, 1123–1127.
(45) Mårsell, E.; Losquin, A.; Svärd, R.; Miranda, M.; Guo, C.; Harth, A.; Lorek, E.; Mauritsson, J.; Arnold, C. L.; Xu, H.; L'Huillier, A.; Mikkelsen, A. Nanoscale Imaging of Local Few-Femtosecond Near-Field Dynamics within a Single Plasmonic Nanoantenna. *Nano Lett.* **2015**, *15*, 6601–6608.
(46) Sun, Q.; Yu, H.; Ueno, K.; Kubo, A.; Matsuo, Y.; Misawa, H. Dissecting the Few-Femtosecond Dephasing Time of Dipole and Quadrupole Modes in Gold Nanoparticles Using Polarized Photoemission Electron Microscopy. *ACS Nano* **2016**, *10*, 3835–3842.
(47) Janssen, A. P.; Akhter, P.; Harland, C. J.; Venables, J. A. High Spatial Resolution Surface Potential Measurements Using Secondary Electrons. *Surf. Sci.* **1980**, *93*, 453–470.
(48) Gronthos, S.; Brahim, J.; Li, W.; Fisher, L. W.; Cherman, N.; Boyde, A.; DenBesten, P.; Robey, P. G.; Shi, S. Stem Cell Properties of Human Dental Pulp Stem Cells. *J. Dent. Res.* **2002**, *81*, 531–535.
(49) Brinkmann, V.; Reichard, U.; Goosmann, C.; Fauler, B.; Uhlemann, Y.; Weiss, D. S.; Weinrauch, Y.; Zychlinsky, A. Neutrophil Extracellular Traps Kill Bacteria. *Science* **2004**, *303*, 1532–1535.
(50) Udagawa, N.; Takahashi, N.; Akatsu, T.; Sasaki, T.; Yamaguchi, A.; Kodama, H.; Martin, T. J.; Suda, T. The Bone Marrow-Derived Stromal Cell Lines MC3T3-G2/PA6 and ST2 Support Osteoclast-Like Cell Differentiation in Cocultures with Mouse Spleen Cells. *Endocrinology* **1989**, *125*, 1805–1813.
(51) Wergin, W. P.; Yaklich, R. W.; Roy, S.; Joy, D. C.; Erbe, E. F.; Murphy, C. A.; Pooley, C. D. Imaging Thin and Thick Sections of Biological Tissue with the Secondary Electron Detector in a Field-Emission Scanning Electron Microscope. *Scanning* **1997**, *19*, 386–395.
(52) Cai, W.; Sainidou, R.; Xu, J.; Polman, A.; García de Abajo, F. J. Efficient Generation of Propagating Plasmons by Electron Beams. *Nano Lett.* **2009**, *9*, 1176–1181.
(53) Bendaña, X.; Polman, A.; García de Abajo, F. J. Single-Photon Generation by Electron Beams. *Nano Lett.* **2011**, *11*, 5099–5103.
(54) García de Abajo, F. J. Optical Excitations in Electron Microscopy. *Rev. Mod. Phys.* **2010**, *82*, 209–275.

DOI: 10.1021/acsnano.7b00548
ACS Nano 2017, 11, 3274–3281

(55) Chung, M. S.; Everhart, T. E. Role of Plasmon Decay in Secondary Electron Emission in the Nearly-Free-Electron Metals. Application to Aluminum. *Phys. Rev. B* **1977**, *15*, 4699−4715.
(56) Henrich, V. E. Role of Bulk and Surface Plasmons in the Emission of Slow Secondary Electrons: Polycrystalline Aluminum. *Phys. Rev. B* **1973**, *7*, 3512−3519.
(57) Werner, W. S. M.; Ruocco, A.; Offi, F.; Iacobucci, S.; Smekal, W.; Winter, H.; Stefani, G. Role of Surface and Bulk Plasmon Decay in Secondary Electron Emission. *Phys. Rev. B: Condens. Matter Mater. Phys.* **2008**, *78*, 233403.
(58) García de Abajo, F. J. The Role of Surface Plasmons in Ion-Induced Kinetic Electron Emission. *Nucl. Instrum. Methods Phys. Res., Sect. B* **1995**, *98*, 445−449.
(59) Rösler, M.; García de Abajo, F. J. Contribution of Charge-Transfer Processes to Ion-Induced Electron Emission. *Phys. Rev. B: Condens. Matter Mater. Phys.* **1996**, *54*, 17158−17165.
(60) Juaristi, J. I.; Rösler, M.; García de Abajo, F. J. Contribution of the Excitation of Conduction Band Electrons to the Kinetic Electron Emission Induced by Slow Ions in Metals. *Phys. Rev. B: Condens. Matter Mater. Phys.* **1998**, *58*, 15838−15846.
(61) Vial, A.; Grimault, A.-S.; Macías, D.; Barchiesi, D.; de la Chapelle, M. L. Improved Analytical Fit of Gold Dispersion: Application to the Modeling of Extinction Spectra with a Finite-Difference Time-Domain Method. *Phys. Rev. B: Condens. Matter Mater. Phys.* **2005**, *71*, 85416.
(62) Goldstein, J. I.; Newbury, D. E.; Echlin, P.; Joy, D. C.; Fiori, C.; Lifshin, E. Image Formation in the Scanning Electron Microscope. In *Scanning Electron Microscopy and X-Ray Microanalysis*; Springer: New York, 1981; pp 123−204.
(63) Frank, L.; Hovorka, M.; Mikmeková, Š.; Mikmeková, E.; Müllerová, I.; Pokorná, Z. Scanning Electron Microscopy with Samples in an Electric Field. *Materials* **2012**, *5*, 2731−2756.
(64) Reimer, L.*Scanning Electron Microscopy; Physics of Image Formation and Microanalysis*; Springer-Verlag: Berlin, Germany, 1998.
(65) Seiler, H. Secondary Electron Emission in the Scanning Electron Microscope. *J. Appl. Phys.* **1983**, *54*, R1−R18.
(66) Lopez, G. P.; Biebuyck, H. A.; Whitesides, G. M. Scanning Electron Microscopy Can Form Images of Patterns in Self-Assembled Monolayers. *Langmuir* **1993**, *9*, 1513−1516.
(67) Seligman, A. M.; Wasserkrug, H. L.; Hanker, J. S. A New Staining Method (OTO) for Enhancing Contrast of Lipid - Containing Membranes and Droplets in Osmium Tetroxide - Fixed Tissue with Osmiophilic Thiocarbohydrazide (TCH). *J. Cell Biol.* **1966**, *30*, 424−432.
(68) Malick, L. E.; Wilson, R. B. Modified Thiocarbohydrazide Procedure for Scanning Electron Microscopy: Routine Use for Normal, Pathological, or Experimental Tissues. *Stain Technol.* **1975**, *50*, 265−269.
(69) Deerinck, T.; Bushong, E.; Lev-Ram, V.; Shu, X.; Tsien, R.; Ellisman, M. Enhancing Serial Block-Face Scanning Electron Microscopy to Enable High Resolution 3-D Nanohistology of Cells and Tissues. *Microsc. Microanal.* **2010**, *16*, 1138−1139.

DOI: 10.1021/acsnano.7b00548
ACS Nano 2017, 11, 3274−3281

NANO LETTERS

Letter

pubs.acs.org/NanoLett

Wireless Communication with Nanoplasmonic Data Carriers: Macroscale Propagation of Nanophotonic Plasmon Polaritons Probed by Near-Field Nanoimaging

Moshik Cohen,*[,†,§] Yossi Abulafia,[§] Dmitry Lev,[∥] Aaron Lewis,[∥] Reuven Shavit,[‡] and Zeev Zalevsky[†,§]

[†]Faculty of Engineering, Bar-Ilan University, Ramat-Gan 52900, Israel

[‡]Department of Electrical and Computer Engineering, Ben-Gurion University of the Negev, Beer-Sheva 84105, Israel

[§]Bar-Ilan Institute for Nanotechnology & Advanced Materials, Ramat-Gan 52900, Israel

[∥]Department of Applied Physics, Selim and Rachel Benin School of Engineering and Computer Science, The Hebrew University, Givat Ram, Jerusalem 9190401, Israel

ABSTRACT: The ability to control the energy flow of light at the nanoscale is fundamental to modern communication and big-data technologies, as well as quantum information processing schemes. However, because photons are diffraction-limited, efforts of confining them to dimensions of integrated electronics have so far proven elusive. A promising way to facilitate nanoscale manipulation of light is through plasmon polaritons—coupled excitations of photons and charge carriers. These tightly confined hybrid waves can facilitate compression of optical functionalities to the nanoscale but suffer from huge propagation losses that limit their use to mostly subwavelength scale applications. With only weak evidence of macroscale plasmon polaritons, propagation has recently been reported theoretically and indirectly, no experiments so far have directly resolved long-range propagating optical plasmon polaritons in real space. Here, we launch and detect nanoscale optical signals, for record distances in a wireless link based on novel plasmonic nanotransceivers. We use a combination of scanning probe microscopies to provide high resolution real space images of the optical near fields and investigate the long-range propagation of nanoscales optical signals. We design our nanotransceivers based on a high-performance nanoantenna, *Plantenna*, hybridized with channel plasmon waveguides with a cross-section of 20 nm × 20 nm, and observe propagation for distances up to 1000 times greater than the plasmon wavelength. We experimentally show that our approach hugely outperforms both waveguide and wireless nanophotonic links. This successful alliance between Plantenna and channel plasmon waveguides paves the way for new generations of optical interconnects and expedites long-range interaction between quantum emitters and photomolecular devices.

KEYWORDS: *Plasmonics, nanoantennas, channel waveguides, wireless, nanoimaging*

The proposed scheme is designed to enable macroscale communication between nanoscale devices utilizing surface plasmon polaritons (SPPs). Hence, we use channel waveguides that confine SPPs to their channel dimensions, which can be as small as several nanometers.[1−8] However, as dimensions decrease, SPPs exhibit increased losses that limit their propagation in waveguides to distances of only few micrometers. To address this fundamental limitation, we convert channel SPPs to optical surface waves that propagate for significantly larger distances on dielectric substrates. A high-efficiency nanoreceiver, designed to convert surface waves to channel SPPs, is placed the remote edge of the system. Figure 1a illustrates the proposed communication nanosystem, which (a) converts light to nanoscale SPPs, (b) propagates SPPs in channel waveguide, (c) converts these SPPs to surface waves and propagatea them for long distance, and (d) excites SPPs from the surface waves at remote locations. As shown in the right-hand side of Figure 1a, laser light illuminates the *Plantenna* to launch SPPs at the waveguide. Second, Plantenna, located at the other edge of the waveguide, converts these SPPs to surface waves that propagate on the substrate. The surface waves are reconverted to SPPs at a remote, Plantenna based nanoreceiver. We use waveguides with a propagation loss of $e^{-\alpha l}$, where the absorption constant $\alpha = (18\ \mu\text{m})^{-1}$ for a channel width of 20 nm at a red wavelength of $\lambda = 633$ nm and l is the propagation length.

In contrast, absorption for wireless links occur only at the antennas and are much lower than for a waveguide. For conventional (e.g., dipole, bowtie) nanoantennas, the propagation loss for wireless links behaves like $(D/l)^2$, where D is the directivity.[9] Here, we show that Plantenna based wireless links hugely outperform both waveguide and conventional nanoantenna based alternatives. Figure 1b presents a 3D model of the nanotransceiver, with zoom in to the Plantenna region

Received: January 19, 2017
Revised: April 25, 2017
Published: May 3, 2017

DOI: 10.1021/acs.nanolett.7b00266
Nano Lett. XXXX, XXX, XXX−XXX

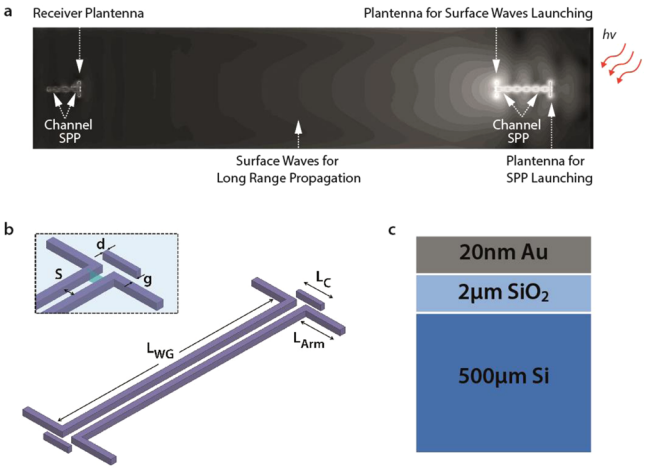

Figure 1. Wireless communications with optical plasmon polaritons. (a) Illustration of the proposed nanoscale communication system. SPP launching Plantenna (right) converts free space light to propagating waveguides SPPs, which are coupled to surface waves by the "Surface Waves Launching Plantenna" for long-range propagation. A Plantenna based nanoreceiver (left) converts the surface waves to channel SPPS at remote distances. (b) 3D model of a Plantenna based plasmonic nanotransceiver. Zoom in to the Plantenna region is shown in the inset c, materials stack up used to fabricate the devices.

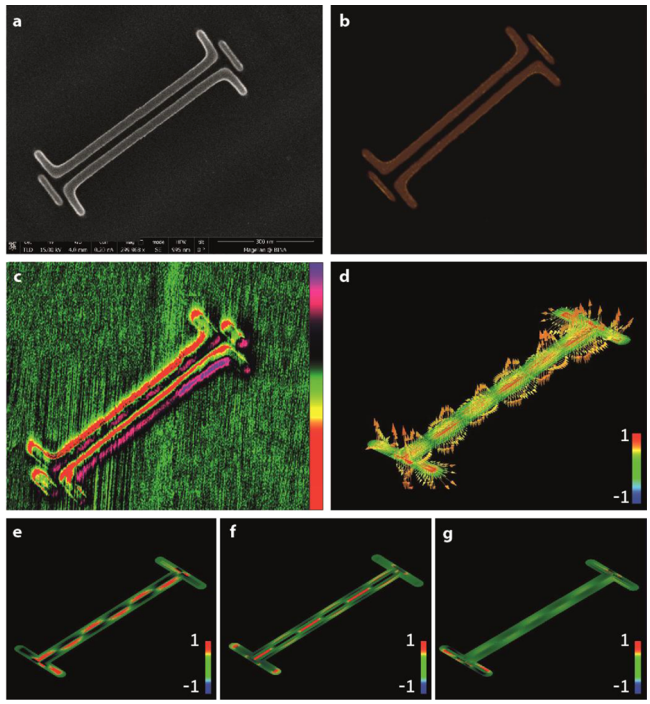

Figure 2. Plantenna-based plasmonic nanotransceiver. (a) High-resolution SEM image of the fabricated nanotransceiver. (b) 3D AFM image of the fabricated nanotransceiver. (c) KPFM under optical illumination analysis of the nanotransceiver. KPFM signal scale bar: ±4.7 V. (d) Numerically calculated optical near-field vector. (e) Numerically calculated optical near-field image showing $\mathrm{Re}(E_z) = |E_z| \cos(\phi_z)$. (f) Numerically calculated optical near-field showing $\mathrm{Re}(E_x)$. (g) Numerically calculated optical near field showing $\mathrm{Re}(E_y)$. Scale bar: 100 nm.

shown in the inset. The physical principle behind the Plantenna invention is the enormous field enhancement and confinement exhibited by resonant, optically illuminated adjacent metallic nanoparticles. These properties, mainly originated from coherent capacitive coupling between the particles, are significantly better than those of isolated nanoparticles. The Plantenna comprised of two metallic nanorods of length L_{Arm}, separated by a nanoscopic gap (s = 10−35 nm), in a dipole arrangement. An additional nanorod, termed director, is placed at much closer proximity of only 7 nm ($g \sim 7$ nm) to the dipole. A detailed analysis on the Plantenna physics, which also includes optimization for high efficiency excitation of channel SPPs, was recently reported.[5] Figure 1c shows the material stack up used in this work, comprised of 20 nm Au layer deposited on a Si on insulator (SOI) wafer (500 μm Si, 2 μm SiO_2), for potential CMOS computability.

For nanofabrication, we use electron beam lithography (EBL), ion beam sputtering (Au, 20 nm), and liftoff. After liftoff, the resist is completely removed, allowing contact mode near-field optical characterization. We fabricated devices comprised of standalone nanotransceivers and complete communication systems. Figure 2a shows a high-resolution scanning electron microscopy (HR-SEM) image of a fabricated nanotransceiver, recorded at beam current of 0.4 nA and low accelerating voltage of 5 kV, for sub 1 nm imaging resolution; corresponding 3D AFM topography is shown in Figure 2b. Nanotransceivers with dimensions of L_{Arm} = 220 nm, L_C = 120 nm, s = 20 nm, g = 7 nm, and L_{WG} = 1.5 μm were fabricated successfully and repeatedly. Figure 2c shows near-field KPFM nanoimaging under illumination with a He−Ne laser (λ_0 = 633 nm), recorded at a set lift height of 30 nm using a high aspect ratio uncoated Si AFM tip with a diameter of 2 nm. As observed, the laser light is efficiently converted to propagating plasmons at the waveguide channel by the Rx (right) Plantenna and then recoupled to surface waves via the Tx (left) Plantenna. Characterized by periodic peaks (purple) in the KPFM signal imaged at the waveguide channel, SPPs with an effective wavelength of 35−150 nm were measured. The experimental results are reproduced by numerical calculation results, presented at the optical frequency of 474 THz (633 nm). The theoretical results are obtained using a high-frequency structure simulator based on the finite element method (FEM).[3−5,10,11] Numerical calculation results of the device are shown in Figure 2d−g, with Figure 2d showing the local near-field vector in 3D, and Figure 2e−g presenting the scalar component of the electrical near-field magnitudes $\mathrm{Re}\{|E_z|\}$, $\mathrm{Re}\{|E_x|\}$, and $\mathrm{Re}\{|E_y|\}$, respectively.

The analysis of a nanoscale wireless communication system that transmits and receives optical plasmon polaritons with a cross section of 20 nm × 20 nm to distance of 12 μm is shown in Figure 3. The system is comprised of a plasmonic nanotransceiver (Figure 1b) and a nanoplasmonic receiver, separated by a distance of 12 μm. Figure 3a presents 3D AFM topography mapping of the nanosystem, where the transceiver is fabricated at the right-hand side and the receiver is located at the left side. To image the near-field structure of long-range plasmon polaritons transfer in real space, we use a combination of KPFM and SNOM. KPFM enables near-field mapping of plasmonic devices with a very high resolution. However, it has limited efficiency in characterizing dielectric devices, mainly since the work function of dielectric materials barely can be modified by optical illumination.[3,4,6,12] Figure 3b shows KPFM analysis of the nanosystem, illuminated by a He−Ne laser (λ = 633 m), linearly polarized in parallel to the dipole orientation and focused to diameter of 700 nm. Channel SPPs are observed at the nanotransceiver channel waveguide, propagate for

DOI: 10.1021/acs.nanolett.7b00266
Nano Lett. XXXX, XXX, XXX−XXX

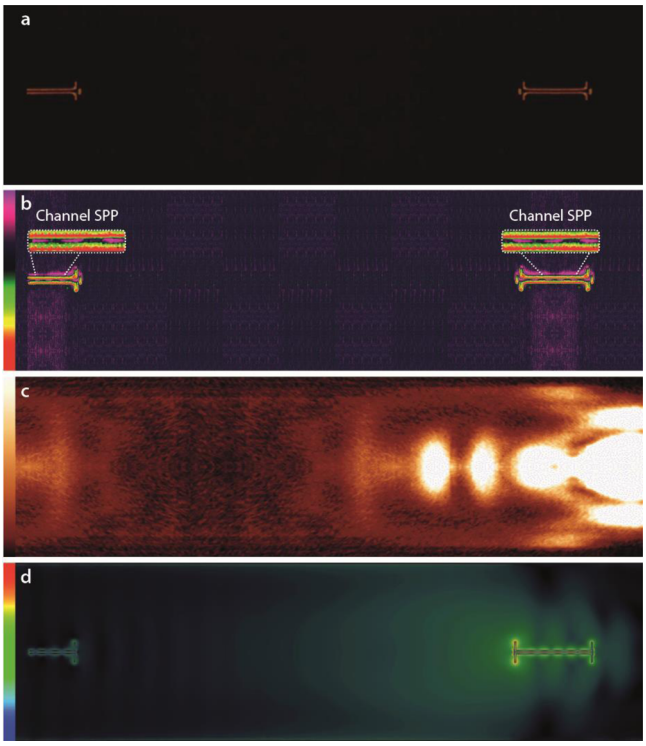

Figure 3. Characterization of the proposed wireless link, demonstrating efficient long-range propagation of tightly confined optical plasmon polaritons. (a) 3D AFM image of the fabricated wireless link system. (b) KPFM under optical illumination analysis of the wireless link system, showing SPPs at the transmission (right) and reception (left) sides; inset—zoom in to the respective waveguide channel. KPFM signal scale bar: ±4.7 V. (c) SNOM analysis of the wireless link system, showing SPPs at the transmission (right) and reception (left) sides, as well as the coupling to surface waves that enable the long-range propagation. (d) Numerically calculated near-field image, showing the complete optical wireless transfer link. Scale bar: 750 nm.

distance of L_{WG} = 1 μm, followed by strong "hot spot" at the Tx Plantenna that converts them to surface waves. A zoom in to the channel region is presented in the inset, clearly showing the periodic structure of the excited SPPs. Remarkably, pronounced SPP excitation is observed at the distanced receiver, which is not illuminated by the laser. Highlighted in the left inset, the channel SPPs at the receiver waveguide are excited by efficient coupling of surface waves to SPP by the receiver Plantenna. The surface waves on the SiO_2 surface are imaged in the near field via SNOM, as shown in Figure 3c. Naturally, SNOM provides lower resolution images compared to KPFM;[3] however, its direct optical imaging mechanism enables mapping of the surface photons that propagate on the dielectric medium, unlike KPFM. Note that the SNOM image exhibits high intensity at the physical locations of the transceiver and receiver, originated by plasmon excitation. Hence, we state that the combination of KPFM and SNOM provides a complementary, complete real-space nanoimaging approach for the characterization of nanoscale wireless communication systems, which facilitates high-resolution nanoimaging of both plasmons and optical surface waves. Numerical calculation results of the nanosystem, presenting the electric near-field magnitude |**E**|, are shown in Figure 3d. Both channel SPPs as well as the surface waves in the dielectric substrate are clearly captured, providing additional confirmation to our approach.

To unambiguously demonstrate the excellent efficiency of our Plantenna based nanosystem, we compare its performances to direct channel waveguiding link[6−8,13] and to wireless link based on dipole nanoantennas.[14−17] For the wireless link configurations (Figure 4a−d) the distance between the transceiver and receiver is 10 μm, and for the direct link (e.g., Figure 4e−f) the waveguide length is 3 μm, limited by fabrication constraints. Figure 4a shows AFM image of our proposed Plantenna based nanosystem, as the corresponding KPFM mapping is shown in Figure 4b with a voltage scale bar of ±4.7 V. Pronounced plasmon excitation is probed at the receiver, evidenced by the modal structure of the field inside

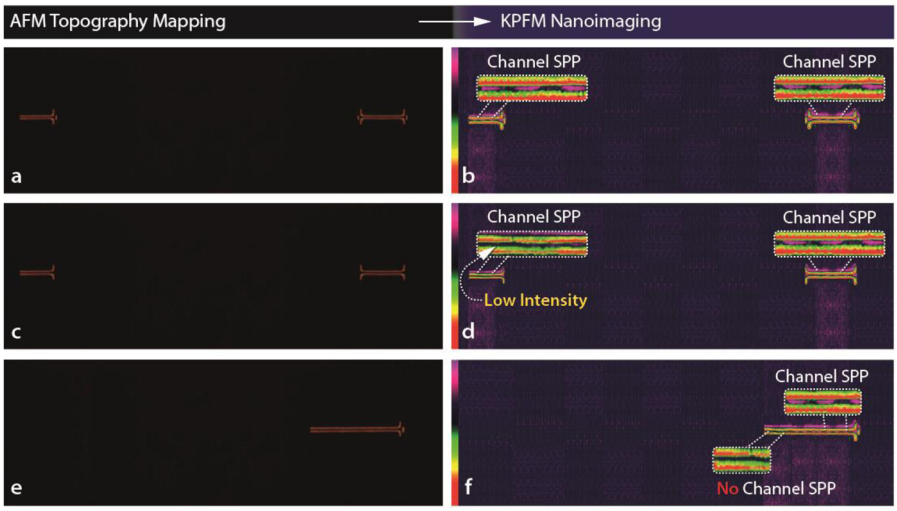

Figure 4. Comparison between nanophotonic links. (a) 3D AFM image of the Plantenna-based wireless link system. (b) KPFM under optical illumination analysis of the Plantenna-based wireless link system; KPFM signal scale bar: ±4.7 V. (c) 3D AFM image of the dipole nanoantenna-based wireless link system. (d) KPFM under optical illumination analysis of the dipole nanoantenna-based wireless link system; KPFM signal scale bar: ±0.5 V. (e) 3D AFM image of channel SPP waveguide with an identical cross section to the waveguides in a−d and 3 μm length. (f) KPFM under optical illumination analysis of the channel SPP waveguide link; KPFM signal scale bar: ±4.7 V; inset (b, d, f): zoom in to the respective waveguide channel. Scale bar: 1 μm.

DOI: 10.1021/acs.nanolett.7b00266
Nano Lett. XXXX, XXX, XXX−XXX

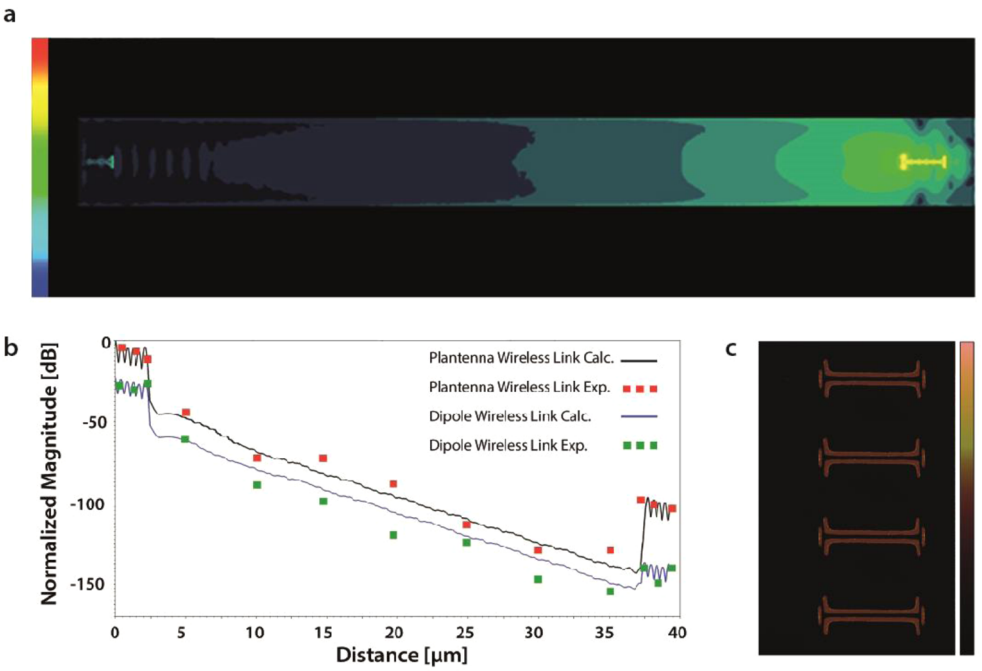

Figure 5. Performance analysis for ultralong propagation distances. (a) Numerically calculated near field image, showing the complete Plantenna-based wireless transfer link with distance of 35 μm between the transmitting and receiving sides. (b) Performance comparison between Plantenna and dipole based wireless links for 35 μm, showing a 30 dB better performance of the Plantenna configuration. (c) 3D AFM image of a three-element Plantenna based transceiver phased array. Scale bar: 200 nm.

the channel which is highlighted in the inset. Figure 4c shows the AFM topography of a wireless link based on dipole nanoantennas, which was recently proposed as an approach for plasmonic energy transfer;[18] the corresponding KPFM image is presented in Figure 4d with a voltage scale bar of ±0.5 V.

We observe plasmon excitation at the transceiver; however, significantly less noticeable intensity is measured at the receiver waveguide (see inset) compared with the Plantenna based architecture. Figure 4e shows a 3D AFM image of a Plantenna integrated with a similar waveguide of 3 μm length, implementing a direct nanoplasmonic link. Unlike the wireless links, the waveguide exhibits much higher propagation loss since it directly propagates tightly confined plasmons that interacts with the metals in their entire guided route.[18] A KPFM map of the direct link is shown in Figure 4f (scale bar ±4.7 V), where the zoom in to the different channel regions is presented in the insets. As seen in the right inset, channel SPPs are excited by the Plantenna and propagate through the waveguide. However, the huge propagation loss makes the waveguide SPPs decay significantly and being practically unobservable after propagating for only 2.5 μm, as seen in the left inset of Figure 4f. This reconfirms the critical, huge losses exhibited in gap plasmon waveguides with nanoscale channels, which hamper their real life applicability. Figure 5a shows the calculated electric near field for a Plantenna based communication nanosystem with a 35 μm distance between the transmitter and receiver. Even for this high separation, plasmon excitation is clearly observed in the receiving device. Dipole nanoantenna is the most popular form of compact couplers to channel waveguide, enabling us to achieve 200 times higher efficiency compared with the case of directly illuminating a base waveguide.[3,4,6,7,10,16] Other types of couplers may use nano-focusing approaches[15] or more complex coupling devices like a Yagi nanoantenna.[19] However, these devices are diffraction limited and cause only marginal improvement compared with the dipole coupler. A comparison between Plantenna and dipole based systems with 35 μm separation is shown in Figure 5b, presenting the normalized near field along a line that connects the transmitter and receiver passing through the centers of both waveguides. The continuous black and blue charts represent the calculated results of a Plantenna and dipole wireless systems, respectively, as the discrete red and green squared dots are the corresponding experimental results. High field values are observed in both Tx and Rx ends, attributed to plasmon enhancement by the nanoantennas. As expected, the field is attenuated linearly when propagates through the SiO_2 substrate.

A quantitative comparison between Plantenna and dipole systems is performed by comparing the SPP magnitude at both receiver waveguides, which serve as input for remote nano-plasmonic circuits[4,12,20] or can be probed by photoelectric detectors. Since both systems are excited with identical sources and use similar plasmon waveguides, this approach is equivalent to calculating the ratio between the wave power of the SPP at the receiver waveguide and the laser source. As seen in Figure 5b, the Plantenna based nanosystem outperforms the dipole configuration by more than 30 dB. Note that from nano-fabrication considerations we use Plantenna with identical dimensions through all of the experiments herein. However, the additional significant efficiency improvement can be achieved using a structural optimization of the different Plantennas as we recently reported.[5] The Plantenna nanosystem can be used to wirelessly transfer optical nanoplasmonic information for macroscale distances using a phased array[21−24] configuration as shown in Figure 5c. By fabricating an array of identical transceivers spaced by $\lambda_0/2$ (λ_0 is the free space wavelength), the emitted surface waves coupled from all of the transceivers can be coherently combined on the surface. Based on the well-known Friis principle,[18,25,26] the phased array architecture enables propagation distances which are linearly scalable with

DOI: 10.1021/acs.nanolett.7b00266
Nano Lett. XXXX, XXX, XXX−XXX

the number of transceivers, paving the way toward efficient wireless nanoplasmonic data and energy transfer for millimeter distances and beyond.

In conclusion, we designed, fabricated, and experimentally characterized a novel high-efficiency nanosystem, capable to wirelessly transfer deeply confined optical plasmon polaritons for chip−scale distances. Our system is architectured for the efficient conversion of nanoscopic SPPs to propagating surface waves and to re-excite SPPs from these surface waves at significantly remote distances. We demonstrate the transmission of optical SPPs in channel waveguides with a cross section of only 20 nm × 20 nm, for distances which are 3 orders of magnitude larger than the plasmon wavelength. On the basis of the Plantenna, a new generation of high-performance nanoantennas with no RF equivalents, our nanosystem hugely outperforms both direct and wireless links based on dipole nanoantennas by more than 30 dB. For the first time, we use a unique combination of scanning probe microscopies to create complete real-space near-field mapping of a long-range nanoplasmonic wireless link at a high spatial resolution. This nanoimaging amalgamation provides valuable synergy needed for mapping both nanoscopic plasmon polaritons as well as macroscopically propagating surface waves. In the quest for reconciling the dimensional mismatch between diffraction-limited photonics and integrated electronics, our results enable new horizons for high integration densities of optical functionalities and interconnects. By using phased array configuration and utilizing degrees of freedom in polarization, frequency and code domains, inter- and intra-chip communications based on ultrafast nanoscale light waves as information carriers can now achieve record performances in terms of speed distance and size. The presented approach of hybridizing Plantenna and channel plasmon waveguides as nanotransceivers is immediately applicable for exploring long-range interaction between single and multiple quantum emitters, while our nanoimaging methodology enables enhanced understanding of exciting near-field phenomena at the nanoscale.

Methods. *AFM and KPFM Measurements.* All measurements were performed at room temperature and free ambient conditions (no vacuum), using a Dimension Icon AFM system with a NanoScope V controller (Bruker). For both AFM and KPFM measurements, we used NanoWorld probes SSS-NCH (SuperSharpSilicon, Noncontact/Tapping mode, High resonance frequency), with a typical diameter of 2 nm, resonance frequency of 320 kHz, and spring constant of 42 N/m. Typically, voltages of 2 V, AC capacitance frequencies of 880 MHz, lift heights of 30−50 nm, and line rates of 0.1 kHz were employed. To map the CPD of the sample, we apply both AC voltage (VAC) and DC voltage (VDC) to the AFM tip. VAC generates oscillating electrical forces between the AFM tip and sample surface, and VDC nullifies the oscillating electrical forces that originated from CPD between tip and sample surface.

Optical Near-Field Measurements. The optical characterization of the plasmonic structures was performed by a MultiView 2000 scanning probe microscope/NSOM system (Nanonics Imaging Ltd.). The SPM head was placed on the stage of an Olympus dual microscope while remaining the optical axis free from above and below. Such a configuration allowed us to bring the cantilevered NSOM tip to the desired position on the sample under an upper objective of 50×. The sample was illuminated with a Liconix diode laser of 785 laser CW light from the bottom and focused on a sample with a 50× objective. We used the bottom piezo scanner of the scanning head to place the desired structures of the sample very accurately relatively to the incoming light of the laser from below. The scan was performed with upper piezo scanner allowing moving only the NSOM tip while the sample remains still. The collection of near field light distribution on the surface was performed in tapping mode with a 200 nm aperture NSOM tips based tuning fork produced by Super Tips (Nanonics Imaging Ltd.). The signal was transmitted through a multimode optical fiber onto an APD. The AFM and NSOM images were collected simultaneously during the scan, allowing to monitor the topography of the desired structure and to correlate it with the near-field optical signal that comes from any particular feature.

Numerical Simulations. The numerical results are obtained by using the software package ANSYS HFSS V15, the industry-standard simulation tool for 3D full-wave electromagnetic field simulation. HFSS solves Maxwell's equations via the finite element method (FEM) using an adaptive mesh refinement process for tailored accuracy requirements. The field's solutions are calculated with the metallic (Ag) plasmonic structures being deposited on a homogeneous SiO_2 substrate. The nanoantenna is illuminated by optical sources at 474 THz (wavelength of 633 nm), which are modeled as focused Gaussian beams with 1 μm characteristic diameter. The electric field is polarized in parallel with the dipole direction, as the wave vector **K** is perpendicular. A selectively dense meshing is assigned in the metallic and waveguiding regions, with a maximum cell size of 1 nm and 750 000 FEM tetrahedral cells. To provide maximum accuracy, the model is terminated as following: the interface with free space is bounded by perfectly matched layer (PML) absorbing boundary conditions (ABC), while the metallic and SiO_2 termination are done via layered impedance (LI) ABC. The minimum number of adaptive meshing iterations was set to 12, with a convergence condition of 1% maximum energy variance between adjacent iterations.

Fabrication. SiO_2/Si sample was spin-coated with poly(methyl methacrylate) (PMMA 950 A2) electron-beam resist providing thickness of 100 nm. The samples coated with PMMA were subsequently baked for 120 s on a hot plate at 180C. The desired pattern was exposed in the PMMA layer using a CRESTEC CABLE-9000C high-resolution electron-beam lithography system using different doses to control line and gap width. Then the samples were developed for 90 s using methyl isobutyl ketone (MIBK) and rinsed with IPA. The samples were subsequently exposed to Ar plasma to etch 10 nm in order to remove leftovers from the pattern, sputtered using BESTEC 2″ DC magnetron to deposit 2 nm Cr and 18 nm Au, and then immersed in 180 Khz ultrasonic bath with NMP for 3 h for resist liftoff.

AUTHOR INFORMATION

Corresponding Author

*E-mail: moshik.cohen80@gmail.com.

ORCID

Moshik Cohen: 0000-0002-7519-9742

Author Contributions

M.C. carried out the theoretical design and analysis, designed the studies, performed the experiments, and wrote the manuscript. Z.Z. and R.S. participated in writing the manuscript and designing the study.

DOI: 10.1021/acs.nanolett.7b00266
Nano Lett. XXXX, XXX, XXX−XXX

Notes

The authors declare no competing financial interest.

■ ACKNOWLEDGMENTS

M.C. acknowledges Olga Girshevitz Yafit from Bar-Ilan Institute for Nanotechnology & Advanced Materials (BINA), for the support in fabricating the reported structures.

■ REFERENCES

(1) Schuller, J. A.; Barnard, E. S.; Cai, W.; Jun, Y. C.; White, J. S.; Brongersma, M. L. *Nat. Mater.* **2010**, *9* (3), 193−204.
(2) Brongersma, M. L.; Shalaev, V. M. *Science* **2010**, *328* (5977), 440−441.
(3) Cohen, M.; Shavit, R.; Zalevsky, Z. *Sci. Rep.* **2015**, *4*, 04096.
(4) Cohen, M.; Zalevsky, Z.; Shavit, R. *Nanoscale* **2013**, *5* (12), 5442−5449.
(5) Cohen, M.; Shavit, R.; Zalevsky, Z. *Sci. Rep.* **2015**, *5*, 17562.
(6) Cohen, M.; Shavit, R.; Zalevsky, Z. In *Planar Waveguides and other Confined Geometries*; Marowsky, G., Ed.; Springer Series in Optical Sciences; Springer: New York, 2015; pp 45−66.
(7) Dionne, J. A.; Sweatlock, L. A.; Atwater, H. A.; Polman, A. *Phys. Rev. B: Condens. Matter Mater. Phys.* **2006**, *73* (3), 035407.
(8) Bozhevolnyi, S. I.; Volkov, V. S.; Devaux, E.; Laluet, J.-Y.; Ebbesen, T. W. *Nature* **2006**, *440* (7083), 508−511.
(9) Dregely, D.; Lindfors, K.; Lippitz, M.; Engheta, N.; Totzeck, M.; Giessen, H. *Nat. Commun.* **2014**, *5*, 4354.
(10) Cohen, M.; Abulafia, Y.; Shavit, R.; Zalevsky, Z. *ACS Nano* **2017**, *11*, 3274.
(11) Carmeli, I.; Cohen, M.; Heifler, O.; Lilach, Y.; Zalevsky, Z.; Mujica, V.; Richter, S. *Nat. Commun.* **2015**, *6*, 7334.
(12) Cohen, M.; Shavit, R.; Zalevsky, Z.; Abulafia, Y. In *CLEO: 2014*; OSA Technical Digest (online); Optical Society of America, 2014; p JTu4A.135.
(13) Lu, H.; Liu, X.; Wang, G.; Mao, D. *Nanotechnology* **2012**, *23* (44), 444003.
(14) Wang, S.; Zhan, Q. *Sci. Rep.* **2016**, *6*, 29626.
(15) Choo, H.; Kim, M.-K.; Staffaroni, M.; Seok, T. J.; Bokor, J.; Cabrini, S.; Schuck, P. J.; Wu, M. C.; Yablonovitch, E. *Nat. Photonics* **2012**, *6* (12), 838−844.
(16) Wen, J.; Romanov, S.; Peschel, U. *Opt. Express* **2009**, *17* (8), 5925−5932.
(17) Andryieuski, A.; Zenin, V. A.; Malureanu, R.; Volkov, V. S.; Bozhevolnyi, S. I.; Lavrinenko, A. V. *Nano Lett.* **2014**, *14* (7), 3925−3929.
(18) Alù, A.; Engheta, N. *Phys. Rev. Lett.* **2010**, *104* (21), 213902.
(19) Solís, D. M.; Taboada, J. M.; Obelleiro, F.; Landesa, L. *Opt. Express* **2013**, *21* (2), 2369−2377.
(20) Dionne, J. A.; Sweatlock, L. A.; Sheldon, M. T.; Alivisatos, A. P.; Atwater, H. A. *IEEE J. Sel. Top. Quantum Electron.* **2010**, *16* (1), 295−306.
(21) Abediasl, H.; Hashemi, H. *Opt. Express* **2015**, *23* (5), 6509−6519.
(22) Cohen, E.; Ruberto, M.; Cohen, M.; Degani, O.; Ravid, S.; Ritter, D. *IEEE Trans. Microwave Theory Tech.* **2013**, *61* (3), 1359−1375.
(23) Sun, J.; Timurdogan, E.; Yaacobi, A.; Hosseini, E. S.; Watts, M. R. *Nature* **2013**, *493* (7431), 195−199.
(24) Maguid, E.; Yulevich, I.; Veksler, D.; Kleiner, V.; Brongersma, M. L.; Hasman, E. *Science* **2016**, *352*, 1202.
(25) Choi, H. S.; Kang, S. Y.; Cho, S. J.; Oh, I.-Y.; Shin, M.; Park, H.; Jang, C.; Min, B.-C.; Kim, S.-I.; Park, S.-Y.; Park, C. S. *Sci. Rep.* **2015**, *4*, 5486.
(26) Yang, Y.; Li, Q.; Qiu, M. *Sci. Rep.* **2016**, *6*, 19490.

DOI: 10.1021/acs.nanolett.7b00266
Nano Lett. XXXX, XXX, XXX−XXX